

Contamination in Dielectric Barrier Discharge Plasmas by Electrode Erosion

Robin De Meyer, Jo Verbeeck, Sara Bals,* and Annemie Bogaerts*

Cite This: *ACS Materials Lett.* 2025, 7, 52–58

Read Online

ACCESS |



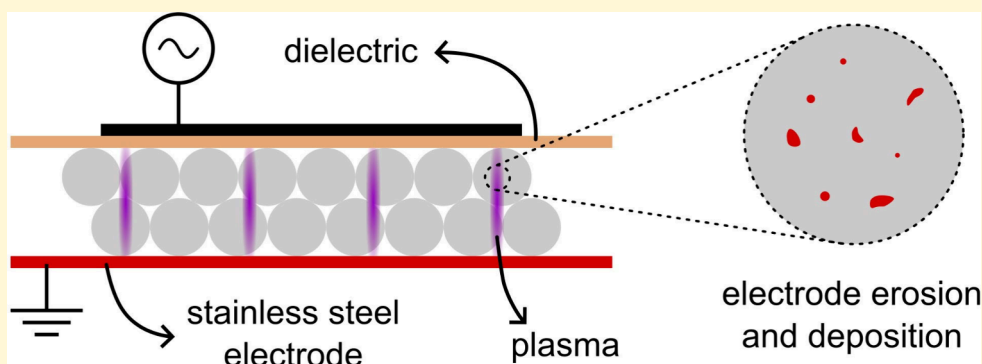
Metrics & More



Article Recommendations



Supporting Information



ABSTRACT: Dielectric barrier discharge plasmas find applications in various fields, including material synthesis and functionalization, plasma catalysis for gas conversion, pollution control, and biological sample treatment. While electrode erosion in these systems has been observed previously, its full implications have remained unclear. In this study, we analyze the effects of electrode erosion by examining alumina spheres exposed to the plasma using electron microscopy for detailed characterization. Our findings show that electrode erosion leads to the deposition of microscopic particles on the materials inside the plasma reactor. Whereas the operating parameters influence the properties of these particles, their formation and deposition is persistent. These electrode particles are an evident source of contamination and may lead to impurities in synthesized materials or altered plasma discharges after long-term operation. Our study highlights the importance of acknowledging the presence and potential impact of these particles for various DBD plasma applications and calls for greater awareness in the scientific community regarding this source of contamination that has been overlooked so far.

A dielectric barrier discharge (DBD) is a type of plasma ignited between two electrodes and is characterized by the presence of a dielectric layer covering at least one of the electrodes, preventing persistent high current arcs from being formed. As a result, DBDs are nonequilibrium plasmas, meaning that the gas temperature is several orders of magnitude lower than the electron temperature.¹ These gentle conditions, combined with the reactive nature of the plasma, partially consisting of excited species, radicals, ions, and electrons, offer a great variety of applications, including surface treatment,^{2–4} (nano)material synthesis and functionalization,^{5–8} catalyst regeneration,^{9,10} plasma catalysis for gas conversion and pollution control,^{11–13} as well as biological and medical applications.^{14–17}

DBDs can operate in various geometries. For many applications, packed-bed DBDs are employed in which the volume between the electrodes (where the plasma is generated) is filled with a packing material. Indeed, this

geometry offers a unique intimate contact between the plasma and the packing material.

Regardless of the geometry, DBDs typically operate in a filamentary mode.¹⁸ This means that generally, the gas volume is not filled with a homogeneous plasma but rather with discrete filaments. These filaments are formed by so-called microdischarges, i.e., short-lived but intense discharges, which can also be observed in the measured current as sharp peaks, with relatively high current densities (up to 1000 A cm⁻²). Microdischarges often majorly contribute to the chemistry in a

Received: September 5, 2024

Revised: November 18, 2024

Accepted: November 20, 2024

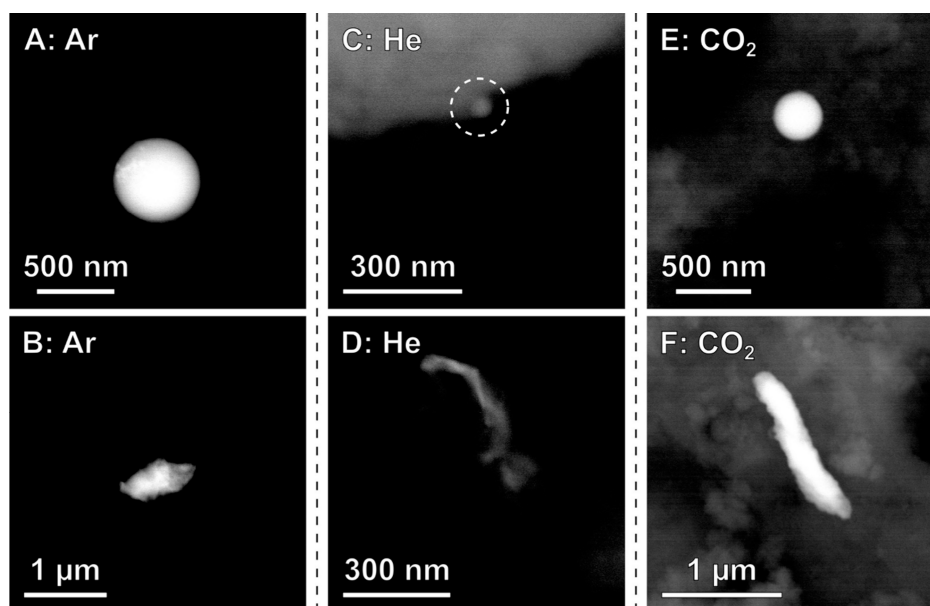


Figure 1. BSE-SEM images of the Ar (A and B), He (C and D), and CO₂ (E and F) samples. The BSE signal highlights the relatively heavy steel particles against a relatively light Al₂O₃ background. Particles with various morphologies were observed, though notably, the Ar (A) and CO₂ (E) samples contained several highly spherical particles.

DBD plasma, but given their short lifetime and discrete nature, gas heating remains limited.¹⁸

The dielectric barrier, especially when employing relatively soft materials, such as polymers, can erode due to the plasma exposure.^{19,20} In addition, erosion of the exposed electrode in surface DBDs was previously described.^{21–24} For example, recently, Nguyen-Smith et al. observed the erosion of the exposed electrode of a surface DBD after operating in air for 60 min.²² By tuning the pulse width of the applied voltage, the authors managed to operate the plasma both in a filamentary and a relatively uniform mode while keeping other discharge parameters such as plasma power similar. Detailed scanning electron microscopy (SEM) and energy dispersive X-ray spectroscopy (EDX) measurements revealed that the electrode was measurably eroded in both cases, although significant differences were observed between the electrodes exposed to a filamentary or a homogeneous plasma. The authors reported that a filamentary discharge locally melts the nickel electrode, with some nickel oxide particles being present both on the electrode and on the dielectric around the eroded area. In contrast, the electrode exposed to a homogeneous discharge did not show any local melting of the electrode. Whereas the oxidation is most likely due to the presence of oxygen, the plasma discharge clearly affects the electrode and the precise discharge characteristics further determine the extent and nature of the erosion.

Given the demonstrated erosion of the electrode due to the plasma discharge and the apparent mobility of the eroded electrode material, the question arises whether a material inside a DBD could possibly be affected by the eroded electrode material. To answer this question, we employed a coaxial DBD, with an exposed stainless steel electrode passing through the center of an Al₂O₃ cylinder, which has the second electrode wrapped around the outside. A schematic of the setup, as well as further technical details, can be found in Section S1.1. The reactor was packed with pristine γ -Al₂O₃ spheres (Sasol) with a diameter of 1.8 mm. To investigate the influence of the discharge characteristics, experiments were

performed in pure Ar, He, and CO₂. Further, to isolate the effect of temperature on the plasma discharge from any potential changes to the packing material itself, every experiment was performed in two phases. First, the plasma was operated for 3 h for Ar and He and for 6 h for CO₂, after which the plasma was stopped. The reactors were then left to cool completely, while continuing the gas flow, without further disturbances. After reaching room temperature, the plasma was operated again for 2 h in the case of Ar and He and 3 h using CO₂ as further discussed below.

After the plasma experiment was completed, the used Al₂O₃ spheres were analyzed by SEM and transmission electron microscopy (TEM). The sample preparation procedure and the parameters used for the SEM and TEM analyses are provided in Section S1.2. In Figure 1, backscattered electron (BSE) SEM images are shown of the surface of the Al₂O₃ spheres exposed to Ar, He, and CO₂ plasma. The BSE-SEM signal is proportional to the mass density of the sample, which allows easy identification of heavier (metallic) particles against the lighter Al₂O₃ background. Note that every particle that is shown or included in further analyses was confirmed to be stainless steel (containing Fe and Cr; and when a high signal-to-noise ratio was obtained, Ni could also be identified; see Section S2.1) using X-ray based spectroscopy. It stands out that both the Ar sample (Figure 1A) and the CO₂ sample (Figure 1E) contain highly spherical stainless steel particles, whereas no such particles were found in the He sample. Further, all samples contain particles of various, seemingly arbitrary, morphology. Moreover, it is striking that the CO₂ sample has a significantly higher fraction of highly spherical particles compared to the Ar sample: 12 out of 19 for CO₂ and 4 out of 24 for Ar.

The SEM analyses enable the investigation of the overall morphology and the composition of the stainless steel particles. However, the SEM lacks the spatial resolution to study the surface structure of the steel particles and may also miss smaller particles. Therefore, high-angle annular dark field scanning transmission electron microscopy (HAADF-STEM)

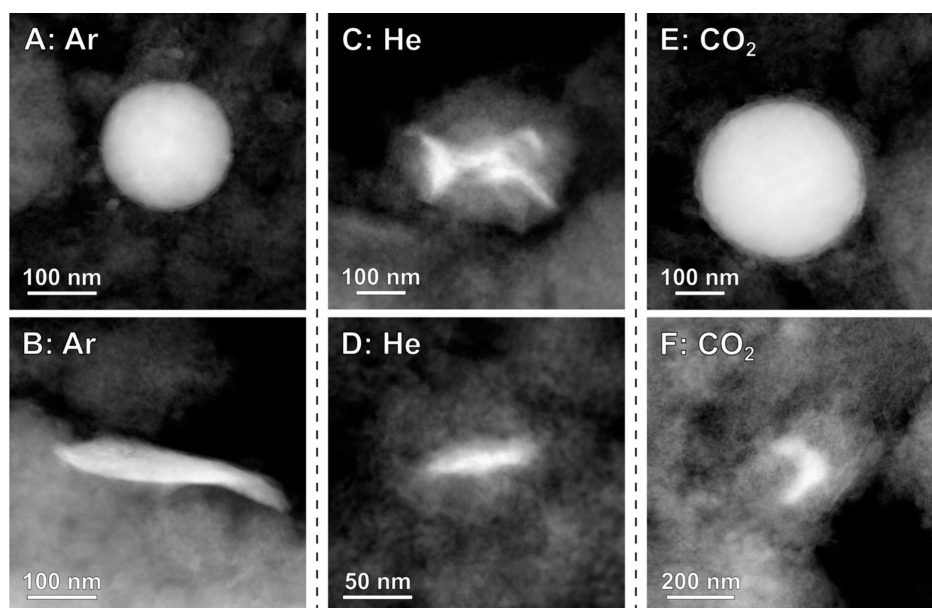


Figure 2. HAADF-STEM images of stainless steel particles in the Ar (A and B), He (C and D), and CO₂ (E and F) samples.

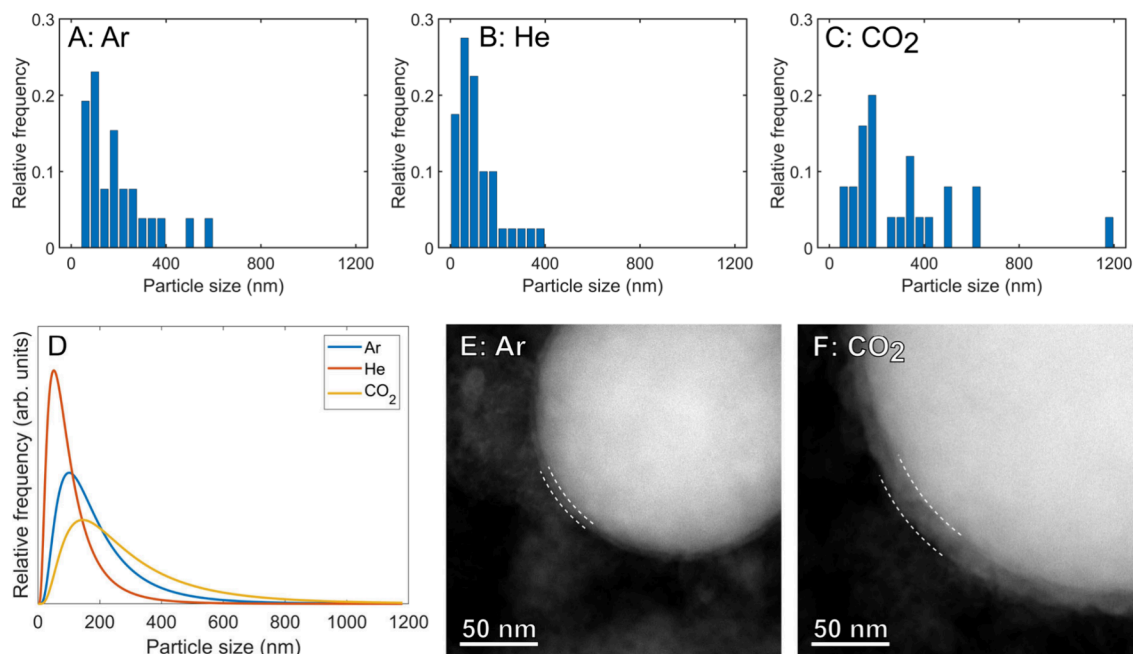


Figure 3. (A–D) Particle size distributions for the stainless steel particles formed in the discharges in various gases based on TEM data. (A–C) Histograms of the particle sizes for Ar (A, 26 particles), He (B, 40 particles), and CO₂ (C, 25 particles). (D) Log-normal distributions. (E and F) Higher magnification images of stainless steel spheres with a thin oxide shell, indicated by the dashed white lines for the Ar (E) and CO₂ (F) samples.

was employed due to its higher spatial resolution compared to SEM. Furthermore, the HAADF signal scales with the projected density of the sample, highlighting the heavier steel particles against the lighter Al₂O₃ background. Figure 2 presents a representative overview of the particles that were observed in the Al₂O₃ samples exposed to the Ar, He, and CO₂ plasma (note that, again, all particles were confirmed to be stainless steel using EDX, consisting of Fe, Cr, and Ni; see Section S2.2).

Based on the TEM images, particle size distributions could be determined. The particle size was defined as the diameter of the smallest circle that encompassed the entire stainless steel

particle in the image. The histograms of these particle sizes are provided in Figures 3A–3C, whereas the fitted log-normal distributions are presented in Figure 3D. Significant differences between the particle sizes from the various samples are observed (see Section S3 for more details). Indeed, the stainless steel particles from the He sample are generally much smaller than the others and more narrowly distributed. The CO₂ sample has the broadest distribution, with the largest particles overall, while the Ar particle size distribution sits somewhere in between He and CO₂.

In addition to the particle size distributions, the increased spatial resolution of TEM enables a more detailed investigation

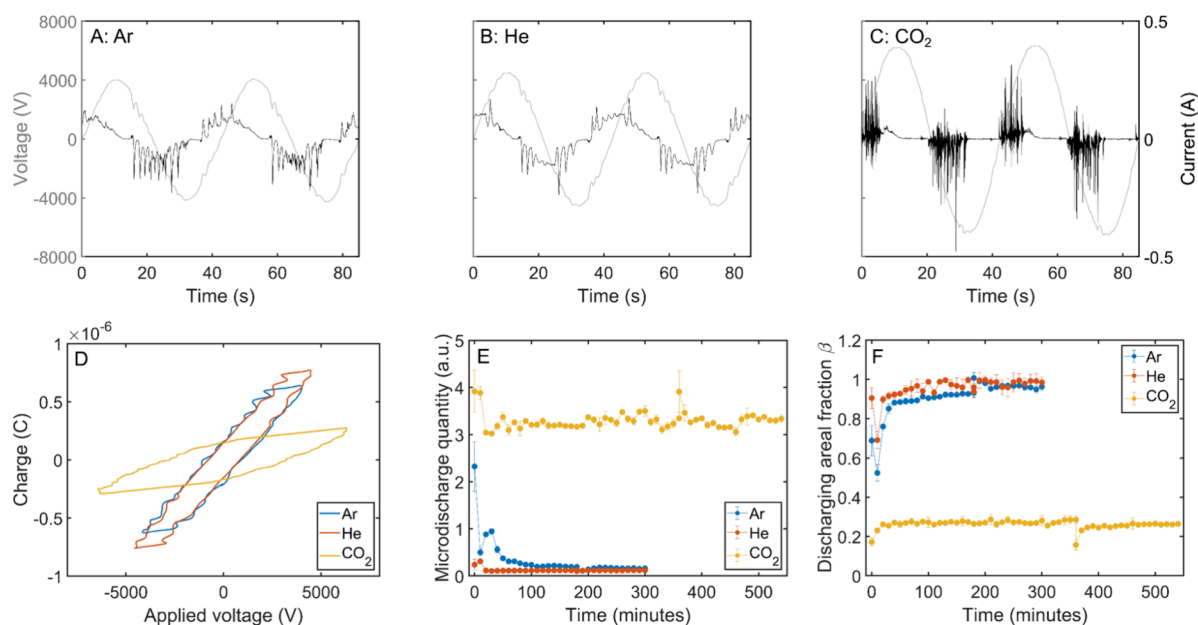


Figure 4. (A–C) Representative voltage and plasma current signals after operating the plasma for 1 h in Ar (A), He (B), and CO₂ (C). (D) Representative Lissajous figures after operating the plasma for 1 h for all gases. (E) Microdischarge quantity over time for all gases. (F) Discharging areal fraction β over time for all gases.

of the individual particles. Higher magnification TEM images in Figures 3E (Ar) and 3F (CO₂) reveal that the spherical stainless steel particles have an oxide shell around their metallic core. Furthermore, the shell in the CO₂ sample is notable thicker compared to the Ar sample (10–15 vs 4–8 nm), which was observed for multiple spherical particles.

Despite the clear observations presented here, it should be noted that the absolute deposition quantity of the eroded particles is low. Bulk characterization techniques were unable to capture an increase in Fe, Cr, or Ni content, as the impurities present in the pristine spheres were too high; thus, no change after the plasma was observed. Furthermore, it was challenging to objectively quantify the number of deposited particles based on, for example, the SEM measurements, as electron microscopy is inherently a local technique and the density of particles on the surface was low. In addition, the number of observed particles varied significantly between spheres, which is understandable as the plasma discharge is not homogeneous throughout the reactor, and thus, spheres in different locations will be affected differently. This prevents a reliable measurement of the extent of erosion in our current system. Nevertheless, the current data offer various insights and enable a comparison between the various discharges.

In order to understand what is causing the formation and deposition of these stainless steel particles as well as which parameters influence the properties of these particles, the plasma discharge should be considered. Therefore, the plasma was electrically characterized, paying attention to two metrics that we believe are highly relevant and representative for the discharge properties: the microdischarge quantity and the discharging areal fraction β . The microdischarge quantity is based on the Fourier transform of the plasma current signal, where the relevant frequency domain is integrated, yielding a value that includes contributions from both the number of microdischarges and their intensity (more details on this analysis can be found in ref 25). The discharging areal fraction β is the fraction of the dielectric barrier actually participating in

the discharge and can be calculated based on the theoretical value of the dielectric capacitance and the measured charge–voltage diagrams (often called Lissajous figures).^{25,26}

As presented in Figure 4, the plasma discharges in the different gases yield varying discharge characteristics. Representative voltage and plasma current signals of the discharge after 1 h of operation are shown in Figures 4A–4C, whereas the measured Lissajous figures (also after 1 h) are presented in Figure 4D. Furthermore, the microdischarge quantity and discharging areal fraction were monitored over time, as presented in Figures 4E and 4F, respectively. Both the visual inspection of the plasma current signal and the quantification of the microdischarges show that the CO₂ discharge is much more filamentary, with drastically more frequent and also more intense microdischarges. In addition, the Lissajous figure (in particular the inclination of the various edges, explained in detail in ref 26) can be analyzed to reveal various discharge properties, such as the discharging areal fraction, as mentioned above. A discharging areal fraction β of less than 0.3 for the CO₂ discharge indicates that barely a quarter of the dielectric barrier actually participates in the discharges. This implies that the power (which is slightly higher for the CO₂ discharge; see Section S4) is dissipated in a smaller volume compared to the discharges in Ar or He, leading to higher local power densities, as is also expected for filamentary discharges. In contrast, the He discharge exhibits opposite properties, for both the microdischarges and the discharging areal fraction β . Indeed, the He plasma yields almost no microdischarges, whereas β approaches 1, indicating that nearly the entire dielectric participates in the discharge and thus that the reactor is completely filled with plasma. The Ar plasma has a discharging areal fraction β similar to that of the He discharge, whereas it exhibits a more filamentary discharge at the start. During the first 1–2 h of operation, the Ar discharge exhibits notably more microdischarges than the He discharge, though this behavior disappears over time. Note that although there are, in fact, changes in the discharge characteristics over time, they are not

due to purely thermal effects. During the first ca. 30 min, the discharge characteristics can vary heavily, as can be expected due to heating of the system.²⁷ However, after again reaching the thermal steady state, the original trends of the discharge characteristics continue as before cooling, indicating there must be an underlying, cumulative effect (more detailed graphs on the cumulative effects are presented in Section S5). This is also why the CO₂ plasma was operated for a longer time than the Ar and He plasma. The discharging areal fraction for Ar and He was already high from the start and increased even more during the first hours of operation. A similar effect was hypothesized for CO₂, as the introduction of metal particles to the outside of the packing can have this effect,²⁵ but it was not observed immediately. Therefore, the plasma was operated for a longer time to allow for the hypothesized cumulative effect to build up. However, even after these additional hours of plasma operation, this trend was not observed.

The quantification of the plasma discharge can offer valuable insights into the underlying mechanisms that are responsible for the formation of these stainless steel particles. For example, we believe that the abundance of the highly spherical particles observed by SEM (see also Figure 1) is directly related to the abundance and intensity of the microdischarges. Indeed, it was already shown by Nguyen-Smith et al. that the microdischarges are able to locally melt the electrode.²² When a small amount of the electrode melts locally, it is possible for a small droplet to be removed, after which it will quickly cool and solidify (as it exits the high-intensity plasma region), thus forming these perfect spheres. This hypothesis is supported by our SEM observations, correlated to the plasma discharge characteristics. As demonstrated in Figure 4, the CO₂ plasma contained many intense microdischarges, leading to this high fraction of spherical steel particles. The Ar discharge was moderately filamentary and only for a limited period of time, explaining why some spherical particles were found but not many. Finally, the He discharge showed almost no microdischarges, which again corroborates the lack of spherical particles.

Regardless of the discharge characteristics, nonspherical stainless steel particles were also observed in every sample. The more randomly shaped particles are most likely formed by different mechanisms, such as sputtering, for example. Ion energies in atmospheric pressure DBDs tend to be rather low, but there may still be ions with sufficient energy to remove material from the exposed electrode surface.^{28–30} While ion mass may have some effect on the sputtering of a material, its influence is not trivial.^{31,32} Moreover, although the molecular weight of CO₂ is slightly higher than that of Ar (44 vs 40 g/mol), it is unlikely that this can explain the differences in particle size distributions, as presented in Figure 3A, especially since CO₂ molecules might split in lighter ions. Rather, the plasma discharge again appears to play a significant role. Indeed, the higher microdischarge quantity, in addition to the higher local power density, is likely intensifying the erosion mechanisms, yielding larger eroded particles for the CO₂ plasma compared to the others. Note that other discharge parameters, such as the burning voltage, frequency, and temperature, may also influence the erosion processes. In addition to sputtering, alternative or additional formation mechanisms for the steel particles caused by, e.g., local heating, oxidation, or even explosive electron emission^{33,34} cannot be ruled out.

Besides the physical effects causing the formation of these particles, chemical effects were also observed, as demonstrated

in Figures 3B and 3C by the stronger oxidation of the exterior of the steel spheres formed in the CO₂ plasma. Indeed, when the CO₂ plasma is sufficiently intense to locally melt the electrode, it is very likely that there will be reactive oxygen species present as well, causing oxidation of the outside layer of the stainless steel. In the Ar plasma, however, no oxygen should be present. Therefore, the lesser oxidation is attributed to oxidation in air during the manipulation of the spheres after plasma operation.

Although there is no direct evidence, oxidation of the steel particles in the CO₂ plasma may explain why the plasma discharge characteristics remained stable over the observed time, contrary to the Ar and He discharges. Indeed, the drop in microdischarge quantity and rise of the discharging areal fraction β is consistent with previous observations for the addition of metal particles to the exterior of the packing spheres, although the loading here is much lower.²⁵ If the exposed stainless steel particles on the spheres would all have oxide surfaces, this may explain why their impact on the plasma discharge is minimal, as the exposed oxide has properties very different from those of the metal. Though this is only a hypothesis, it does highlight the complexity of the system, making it very important to further our understanding of all processes taking place during the experiment.

It should be noted that, in addition to the materials described here, we also observed stainless steel particles on the packing material after plasma operation for other DBD reactors with very different specifications (see Section S6, including a sample from ref 35). Moreover, very small nanoparticles (down to 2–3 nm) were found in a carbon matrix after generating pure CH₄ plasma in an empty DBD (see Section S7). Hence, despite the large variety in reactor geometries and operating conditions, the erosion and subsequent deposition of an exposed metal electrode in a DBD seems inevitable. Therefore, it is crucial that this phenomenon is known and understood. Whether this effect is problematic, or to what extent, depends heavily on the desired application. For example, when treating biological samples, such as seeds or even food, a small number of metal nanoparticles may already pose toxicity risks.³⁶ In addition, when treating or synthesizing materials using DBDs, the deposition of these particles may introduce undesired impurities. Also in plasma catalysis, this effect may be drastic, especially when considering long-term operation with the aim of further scale up and industrialization. Indeed, as discussed earlier, the deposition of metal particles on the packing material is likely to have an effect on the discharge characteristics, which, in turn, will alter the overall performance. Moreover, the introduction of (overlooked) metal(oxide) particles may offer catalytically active sites that could further steer the reactions in a different direction over time. Therefore, it is crucial that researchers are aware of this effect, so it can be taken into account when interpreting results and designing novel systems. Note that this issue could be addressed by employing a double DBD, where both electrodes are covered by a dielectric. Although this would prevent the formation and deposition of steel particles, the dielectric material may erode to some extent as well, as was recently shown by Wang et al. for surface DBDs.²¹ Moreover, covering the second electrode will alter the plasma discharge, which may limit the overall performance of the system.³⁷ Whether the use of a double DBD is beneficial depends on the precise application, finding a balance between the deposition of the

electrode material and the alteration of the discharge with potential effects on the overall performance.

In conclusion, while dielectric barrier discharges (DBDs) are generally regarded as gentle plasmas, our study demonstrates that the exposed stainless steel electrodes undergo erosion. This erosion leads to the deposition of stainless steel particles on the packing material, making it a significant source of contamination. Our results indicate that the plasma discharge parameters strongly influence the particles' size, shape, and surface oxidation, yet the formation of these particles occurs consistently across different operating conditions, suggesting that this issue is widespread.

The presence of these particles must be considered in all potential applications such as material synthesis or functionalization. In catalytic applications, stainless steel particle contamination may obscure experimental results and ultimately affect the plasma discharge, thereby impacting the overall performance. Additionally, when DBD plasmas are used for treating biological systems, such as seeds or food, the presence of stainless steel particles could pose serious health risks, emphasizing the importance of understanding and mitigating this effect in practical applications.

■ ASSOCIATED CONTENT

SI Supporting Information

The Supporting Information is available free of charge at <https://pubs.acs.org/doi/10.1021/acsmaterialslett.4c01828>.

Experimental method details, energy dispersive X-ray spectra, details on the fit of the particle size distributions, plasma power over time, discharge characteristics over time, data on steel particles from other reactors, and steel particles in a carbon matrix formed in an empty reactor (PDF)

■ AUTHOR INFORMATION

Corresponding Authors

Sara Bals – Research Group EMAT, Department of Physics and Nanolab Centre of Excellence, University of Antwerp, 2020 Antwerp, Belgium; orcid.org/0000-0002-4249-8017; Email: sara.bals@uantwerpen.be

Annemie Bogaerts – Research Group PLASMANT, Department of Chemistry, University of Antwerp, 2610 Antwerp, Belgium; orcid.org/0000-0001-9875-6460; Email: annemie.bogaerts@uantwerpen.be

Authors

Robin De Meyer – Research Group PLASMANT, Department of Chemistry, University of Antwerp, 2610 Antwerp, Belgium; Research Group EMAT, Department of Physics and Nanolab Centre of Excellence, University of Antwerp, 2020 Antwerp, Belgium; orcid.org/0000-0002-2390-7233

Jo Verbeeck – Research Group EMAT, Department of Physics, University of Antwerp, 2020 Antwerp, Belgium

Complete contact information is available at:

<https://pubs.acs.org/doi/10.1021/acsmaterialslett.4c01828>

Author Contributions

CRedit: Robin De Meyer conceptualization, data curation, formal analysis, investigation, methodology, software, validation, visualization, writing - original draft; Johan Verbeeck funding acquisition, methodology, resources, supervision,

writing - review & editing; Sara Bals funding acquisition, methodology, resources, supervision, writing - review & editing; Annemie Bogaerts funding acquisition, methodology, resources, supervision, writing - review & editing.

Notes

The authors declare no competing financial interest.

■ ACKNOWLEDGMENTS

The authors acknowledge Joran Van Turnhout and Rani Vertongen for kindly providing us with the additional samples they used in their different reactors. This research was supported through long-term structural funding (Methusalem FFB15001C) and by the European Research Council (ERC) under the European Union's Horizon 2020 Research and Innovation Programme with Grant 810182 (SCOPE ERC Synergy Project) and with Grant 815128 (REALNANO).

■ REFERENCES

- (1) Fridman, A.; Kennedy, L. *Plasma Physics and Engineering*; CRC Press, 2016. DOI: [10.1201/b11728](https://doi.org/10.1201/b11728)
- (2) Borcia, G.; Anderson, C. A.; Brown, N. M. D. Dielectric barrier discharge for surface treatment: application to selected polymers in film and fibre form. *Plasma Sources Sci. Technol.* **2003**, *12*, 335–344.
- (3) Wagner, H.-E.; et al. The barrier discharge: basic properties and applications to surface treatment. *Vacuum* **2003**, *71*, 417–436.
- (4) Lapena, M. H.; Lopes, C. M. A. Improvement of aerospace thermoplastic composite adhesion to coating with dielectric barrier discharge atmospheric pressure plasma surface treatment. *Plasma Processes & Polymers* **2023**, *20*, No. 2200081.
- (5) Mierczynski, P.; Mierczynska-Vasilev, A.; Szykowska-Jozwik, M.; Vasilev, K. Atmospheric plasma in the preparation and pre-treatment of catalytic materials – A mini review. *Catal. Commun.* **2024**, *187*, No. 106839.
- (6) Wang, Z.; et al. Catalyst Preparation with Plasmas: How Does It Work? *ACS Catal.* **2018**, *8*, 2093–2110.
- (7) Khoja, A. H.; Tahir, M.; Amin, N. A. S. Cold plasma dielectric barrier discharge reactor for dry reforming of methane over Ni/ γ -Al₂O₃-MgO nanocomposite. *Fuel Process. Technol.* **2018**, *178*, 166–179.
- (8) He, J.; et al. Dielectric barrier discharge plasma for nanomaterials: Fabrication, modification and analytical applications. *TrAC Trends in Analytical Chemistry* **2022**, *156*, No. 116715.
- (9) HafezKhibani, N.; Fathi, S.; Shokri, B.; Hosseini, S. I. A novel method for decoking of Pt–Sn/Al₂O₃ in the naphtha reforming process using RF and pin-to-plate DBD plasma systems. *Applied Catalysis A: General* **2015**, *493*, 8–16.
- (10) Kim, M.; Jeoung, J.; Kim, J.; Ha, K.-S. Regeneration of deactivated H-ZSM-5 for aromatization by dielectric barrier discharge plasma. *Applied Catalysis A: General* **2019**, *575*, 214–222.
- (11) Bogaerts, A.; et al. The 2020 plasma catalysis roadmap. *J. Phys. D: Appl. Phys.* **2020**, *53*, No. 443001.
- (12) Ollegott, K.; Wirth, P.; Oberste-Beulmann, C.; Awakowicz, P.; Muhler, M. Fundamental Properties and Applications of Dielectric Barrier Discharges in Plasma-Catalytic Processes at Atmospheric Pressure. *Chemie Ingenieur Technik* **2020**, *92*, 1542–1558.
- (13) Bogaerts, A.; Neyts, E. C.; Guaitella, O.; Murphy, A. B. Foundations of plasma catalysis for environmental applications. *Plasma Sources Sci. Technol.* **2022**, *31*, No. 053002.
- (14) Nishime, T. M. C.; Wannicke, N.; Horn, S.; Weltmann, K.-D.; Brust, H. A Coaxial Dielectric Barrier Discharge Reactor for Treatment of Winter Wheat Seeds. *Applied Sciences* **2020**, *10*, 7133.
- (15) Roy, S.; Choudhury, B.; Johnson, J.; Schindler-Tyka, A. Application of dielectric barrier discharge for improving food shelf life and reducing spoilage. *Sci. Rep.* **2021**, *11*, 19200.
- (16) Laroque, D. A.; Seó, S. T.; Valencia, G. A.; Laurindo, J. B.; Carciofi, B. A. M. Cold plasma in food processing: Design,

mechanisms, and application. *Journal of Food Engineering* **2022**, *312*, No. 110748.

(17) Daeschlein, G.; et al. Skin decontamination by low-temperature atmospheric pressure plasma jet and dielectric barrier discharge plasma. *Journal of Hospital Infection* **2012**, *81*, 177–183.

(18) Brandenburg, R. Dielectric barrier discharges: progress on plasma sources and on the understanding of regimes and single filaments. *Plasma Sources Sci. Technol.* **2017**, *26*, No. 053001.

(19) Hanson, R. E.; Houser, N. M.; Lavoie, P. Dielectric material degradation monitoring of dielectric barrier discharge plasma actuators. *J. Appl. Phys.* **2014**, *115*, No. 043301.

(20) Bian, D.; Wu, Y.; Long, C.; Lin, B. Effects of material degradation on electrical and optical characteristics of surface dielectric barrier discharge. *J. Appl. Phys.* **2018**, *124*, No. 183301.

(21) Wang, A.; et al. The time evolution of electrical and thermodynamic characteristics of surface dielectric barrier discharge caused by dielectric degradation. *J. Phys. D: Appl. Phys.* **2024**, *57*, No. 445203.

(22) Nguyen-Smith, R. T.; et al. μ s and ns twin surface dielectric barrier discharges operated in air: from electrode erosion to plasma characteristics. *Plasma Sources Sci. Technol.* **2022**, *31*, No. 035008.

(23) Selivonin, I.; Lazukin, A.; Moralev, I.; Krivov, S.; Roslyakov, I. Erosion of the sputtered electrodes in the surface barrier discharge. *J. Phys.: Conf. Ser.* **2019**, *1394*, No. 012027.

(24) Selivonin, I.; Moralev, I. Microdischarges properties in sDBD: the role of the exposed electrode oxidation. *Plasma Sources Sci. Technol.* **2020**, *30*, No. 035005.

(25) De Meyer, R.; et al. Importance of plasma discharge characteristics in plasma catalysis: Dry reforming of methane vs. ammonia synthesis. *Chemical Engineering Journal* **2024**, *488*, No. 150838.

(26) Peeters, F. J. J.; van de Sanden, M. C. M. The influence of partial surface discharging on the electrical characterization of DBDs. *Plasma Sources Science and Technology* **2015**, *24*, No. 015016.

(27) Ráhel, J.; Szalay, Z.; Čech, J.; Morávek, T. On spatial stabilization of dielectric barrier discharge microfilaments by residual heat build-up in air. *Eur. Phys. J. D* **2016**, *70*, 92.

(28) Neyts, E. C. Plasma-Surface Interactions in Plasma Catalysis. *Plasma Chem. Plasma Process* **2016**, *36*, 185–212.

(29) Babaeva, N. Y.; Kushner, M. J. Ion energy and angular distributions onto polymer surfaces delivered by dielectric barrier discharge filaments in air: I. Flat surfaces. *Plasma Sources Sci. Technol.* **2011**, *20*, No. 035017.

(30) Babaeva, N. Y.; Ning, N.; Graves, D. B.; Kushner, M. J. Ion activation energy delivered to wounds by atmospheric pressure dielectric-barrier discharges: sputtering of lipid-like surfaces. *J. Phys. D: Appl. Phys.* **2012**, *45*, No. 115203.

(31) Yamamura, Y.; Tawara, H. Energy dependence of ion-induced sputtering yields from monatomic solids at normal incidence. *Atomic Data and Nuclear Data Tables* **1996**, *62*, 149–253.

(32) Mauchamp, N. A.; Hamaguchi, S. Why are physical sputtering yields similar for incident ions with different masses?—physical sputtering yields of the Lennard–Jones system. *J. Phys. D: Appl. Phys.* **2022**, *55*, No. 225209.

(33) Mesyats, G. A. Ecton mechanism of the vacuum arc cathode spot. *IEEE Trans. Plasma Sci.* **1995**, *23*, 879–883.

(34) Mesyats, G. A. Ecton Mechanism of the Cathode Spot Phenomena in a Vacuum Arc. *IEEE Trans. Plasma Sci.* **2013**, *41*, 676–694.

(35) Vertongen, R.; et al. Sorption-Enhanced Dry Reforming of Methane in a DBD Plasma Reactor for Single-Stage Carbon Capture and Utilization. *ACS Sustainable Chem. Eng.* **2024**, *12*, 10841–10853.

(36) Egbuna, C.; et al. Toxicity of Nanoparticles in Biomedical Application: Nanotoxicology. *Journal of Toxicology* **2021**, *2021*, 1–21.

(37) Mei, D.; et al. CO₂ reforming of CH₄ in single and double dielectric barrier discharge reactors: Comparison of discharge characteristics and product distribution. *Journal of CO₂ Utilization* **2021**, *53*, No. 101703.